Supporting Information

Experimental Section

Synthesis and crystal growth: All the chemical reagents and solvents were purchased and used without further purification. Compound $EA_4Pb_3Br_{10}$ (EA is ethylamine) was synthesized from the HBr solution containing an appropriate amount of $Pb(Ac)_2{\cdot}3H_2O$ and ethylamine. Firstly, $Pb(Ac)_2{\cdot}3H_2O$ (~ 6 mmol) was dissolved in HBr solution (20 ml) by heating under constant magnetic stirring to a colorless solution. And then, ethylamine (~ 10 mmol) was added. Subsequently, the saturated solutions were prepared after the continuous stirring. The crystallization temperature should be controlled near 43 ℃, and the high-quality yellow block crystals with large dimension ($52 \times 4 \times 2$ mm³) can be obtained by slowly cooling (1℃ / day) the above solution from 80 ℃ to 30 ℃.

Powder X-ray diffraction. Powder X-ray diffraction (PXRD) data were measured on a Rigaku Mini Flex 600 Powder X-ray diffractometer at room temperature to confirm the phase purity of the crystal, and the diffraction patterns were collected in the 2ɵ range of 5° - 50° with a step size of 0.02°.

Morphology Characterization. The atomic force microscope (AFM) and scanning electron microscope (SEM) images of the surface of **1** SC were collected on a Bruker Dimension ICON atomic force microscope and a JEOL JSM6700-F field emission scanning electron microscope, respectively. In terms of details, AFM measurements were performed using silicon SPM probes with a tip radius of curvature of 2 nm, a spring constant of 0.4 N/m, and a resonant frequency of 70 kHz.

Thermal analysis. Thermogravimetric analysis (TGA) was performed on STA449C Thermal Analyser ranging from room temperature to 1200 ℃ with a heating rate of 15 ℃/min.

Optical absorption spectra Measurement: The diffuse reflection spectrum between 200 and 800 nm of **1** powder was measured by a PerkinElmer Lambda 950 UV-vis-NIR spectrophotometer with $BaSO_4$ as reference.

Ferroelectric Measurement. A ferroelectric analyzer (Radiant Precision Premier II) was used to document the hysteresis loops in relation to the polarization and electric field (*P-E*). The single crystal of **1** was submerged in silicone oil to measure the *P-E* hysteresis loops.

Computational Details. The single-crystal structural data of **1** were employed for theoretical calculations. The partial density of states (PDOS) was calculated via density functional theory (DFT) implemented in the CASTEP total energy code. The exchange-correlation effects were treated using the Perdew–Burke–Ernzerhof (PBE) functional within the generalized gradient approximation (GGA) framework. The interactions between ionic cores and valence electrons were described using norm-conserving pseudopotentials.

Single-Crystal XRD Simulations. Simulations of XRD diffraction peaks were performed using the single-crystal structural data of **1** via Mercury software (Cambridge Crystallographic Data Center Inc.). The crystallographic information file (CIF) file of **1** was imported into Mercury software, and the simulated powder XRD pattern was generated by selecting the powder pattern function.

Piezoelectric Measurements. Piezoelectric measurements were conducted using a quasi-static d_{33} meter (ZJ-1AN).

Photoelectric Measurement. The Ag electrode has a thickness of 0.5 mm (**Figure S17a**), and the inter-electrode distances are 1.5 mm and 1.6 mm along the polar *c*-axis and *a*-axis, respectively, as illustrated in Figure **S17b**. Two symmetric Ag electrodes were deposited on the flat surface of the bulk single crystal, which defines a 2.0 mm² active sensing area for the single-crystal (SC) detector. Detailed schematic diagrams of the optical setup (**Figures S19 – S20**), along with a comprehensive table listing the model numbers and corresponding parameters of optical components (*e.g.*, polarizer, 1/4 λ plate, 405 nm laser source) (**Table S1**), have been shown. High-precision Keithley 6517B electrometers were employed to measure current in environments of both brightness and darkness. The THORLABS 405 nm pigtailed laser diode was employed for light illumination. The incident light power was regulated using the light power meter.

Prior to formal testing, we conducted a rigorous calibration of the incident light polarization state to ensure the reliability of subsequent results (**Figure S19**). The calibration process is as follows: natural light emitted by the light source is first converted into linearly polarized light by the polarizer. This linearly polarized light then impinges on the 1/4λ plate and is modulated into the target circularly polarized light (CPL). An analyzer is placed downstream of the 1/4λ plate; with the analyzer's rotation, the intensity of light is captured at varying rotational angles ranging from 0° to 360°. (**Figure S21**). The measured average power $\bar{P}$ = 17.67 mW, maximum power $P_{\max}$ = 17.70 mW, and minimum power $P_{\min}$ = 17.58 mW. The calculation is as follows:

$$\text{Relative fluctuation amplitude} = \frac{P_{max} - P_{min}}{\bar{P}} \times 100\% = \frac{17.70 - 17.58}{17.67} \times 100\% = 0.7\%$$

It shows that the relative fluctuation of the incident power was ~ 0.7% over the full rotation range, indicating the stability of the power. For an ideal CPL, the light intensity remains relatively constant after passing through the rotating analyzer. (Website: https://www.youtube.com/watch?v=P0asuzX4x-Q)

Figure S19 clearly depicts the spatial arrangement of each component and the light propagation path within the polarization-dependent photoelectric testing system. During the CPL detection test, which is designed to characterize the polarization discrimination capability of the detector sample, a polarizer and a 1/4λ plate are incorporated into the optical path for evaluating the response characteristics of the sample to circularly polarized light with distinct handedness. Use a power meter to determine the power required for testing. To match the spatial orientation between the crystal's helical optical axis and its *ac* plane, the modulated CPL was incident along one of the two optical axes of the *mm*2 point group single crystal (**Figure S21**).[1] This configuration enables selective interaction between the CPL and the crystal's intrinsic helical structure, thereby achieving highly sensitive discrimination of the light's helicity.[2]

Figures

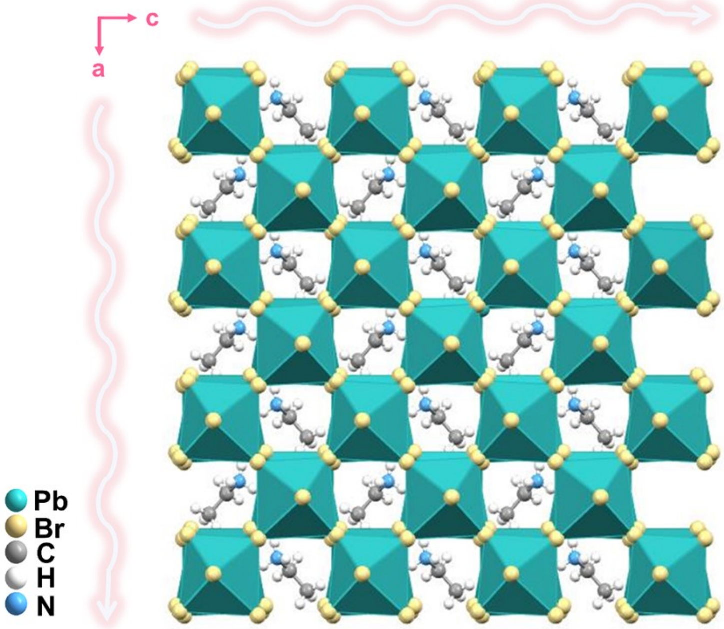

Figure S1. The structure of **1** at FEP viewed along the *b*-axis.

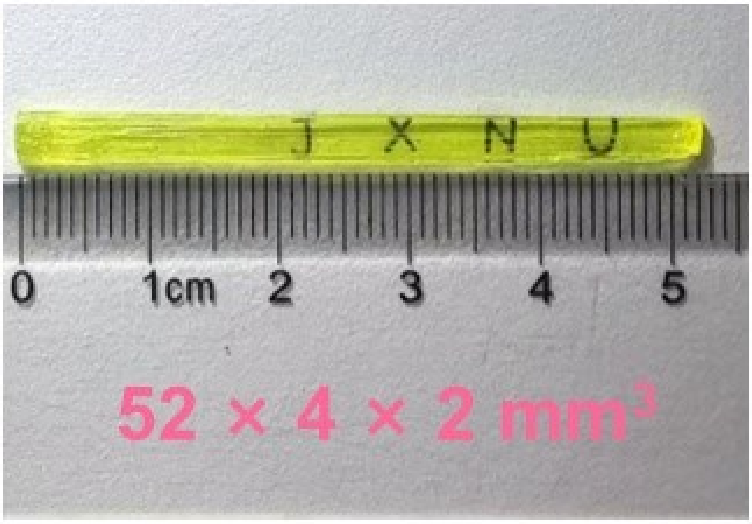

Figure S2. The inch-size crystal of **1** with the size of 52 × 4 × 2 mm^3.

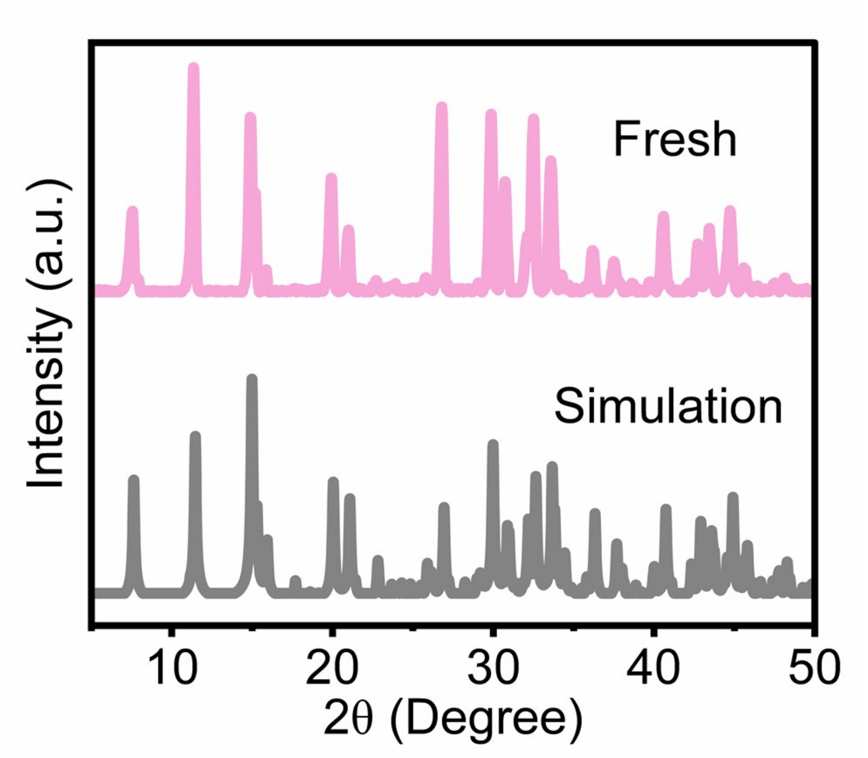

Figure S3. Powder X-ray diffraction patterns of **1**.

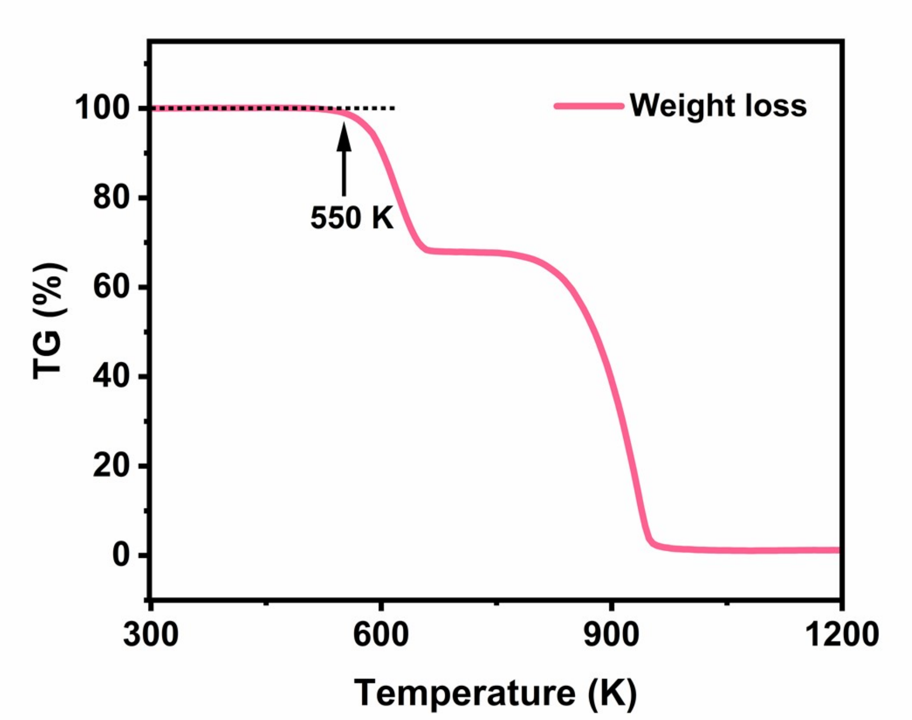

Figure S4. TG curve of **1** powders.

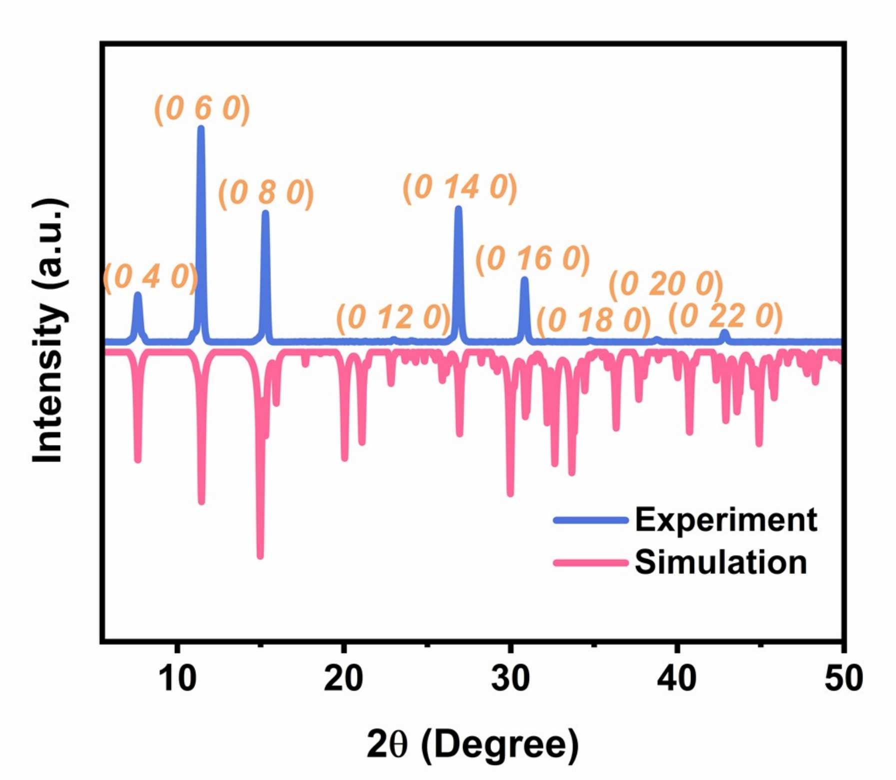

Figure S5. XRD scan of the top facet of **1** SC.

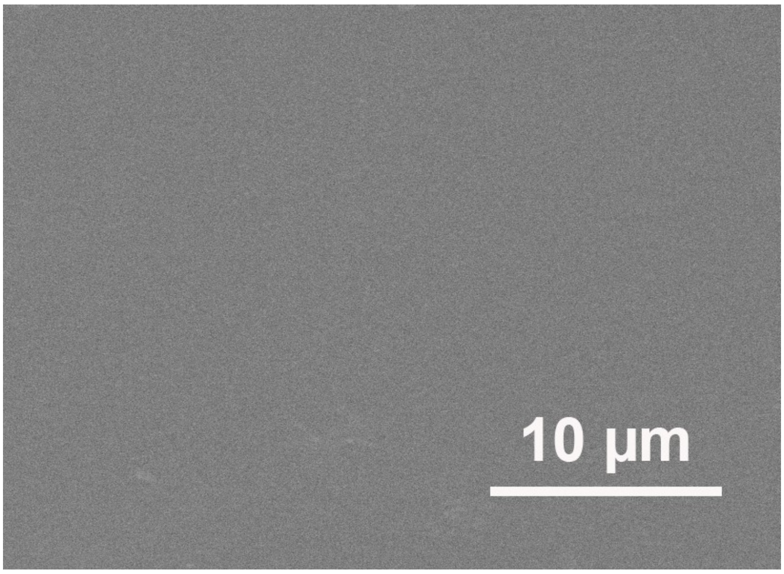

Figure S6. The SEM image of **1** crystal.

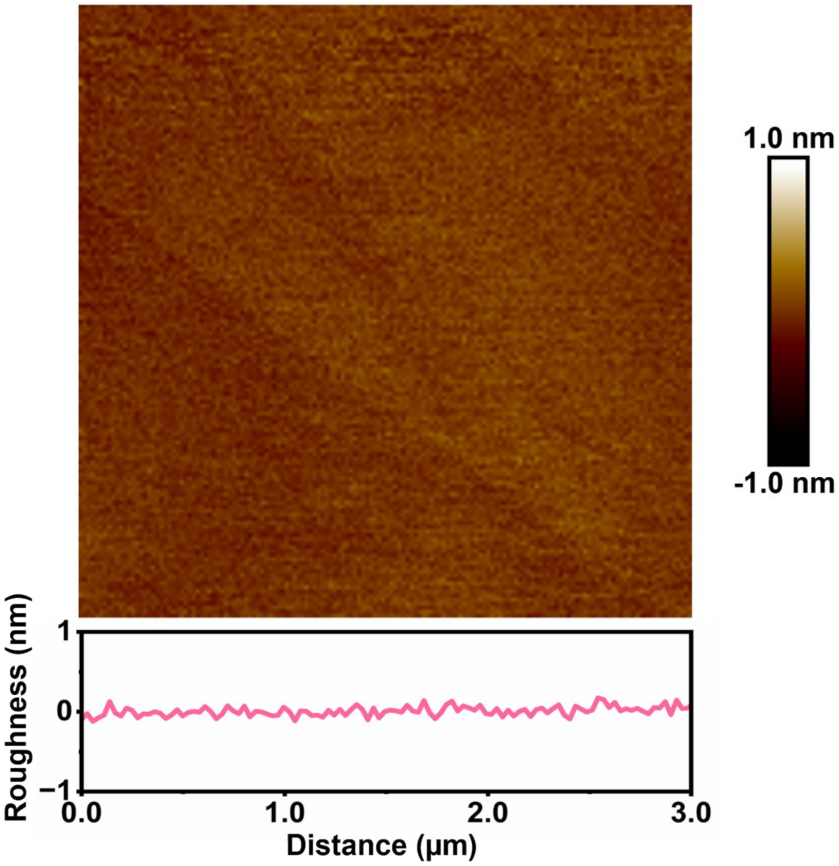

Figure S7. The AFM image of **1** crystal.

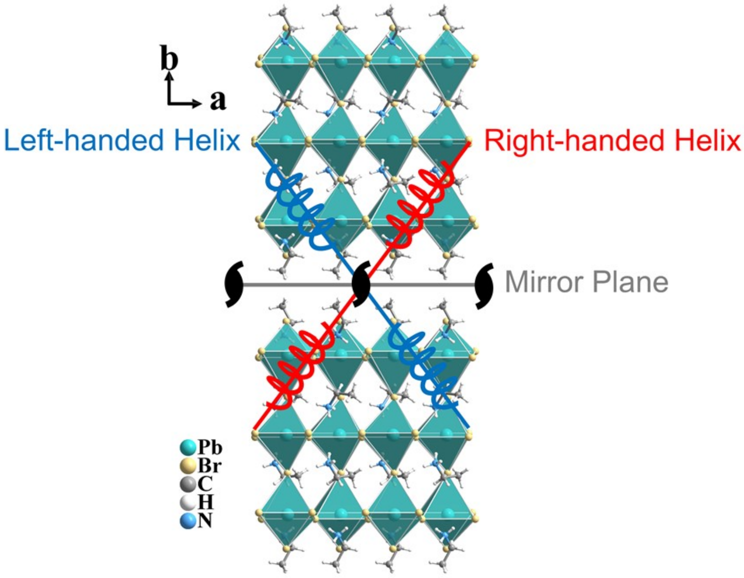

Figure S8. The relationship between the left-handed helix and right-handed helix relative to the mm2 symmetry plane in the **1** crystal.

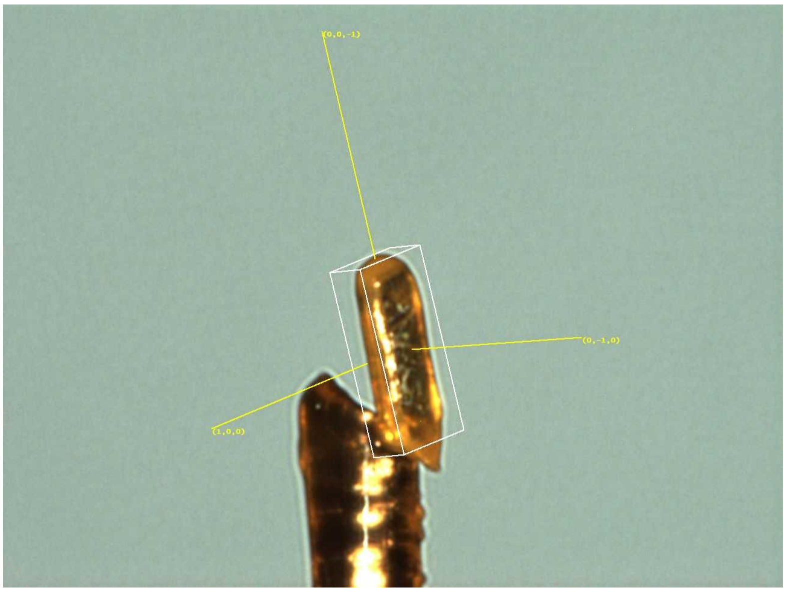

Figure S9. The crystal orientation of **1** SC.

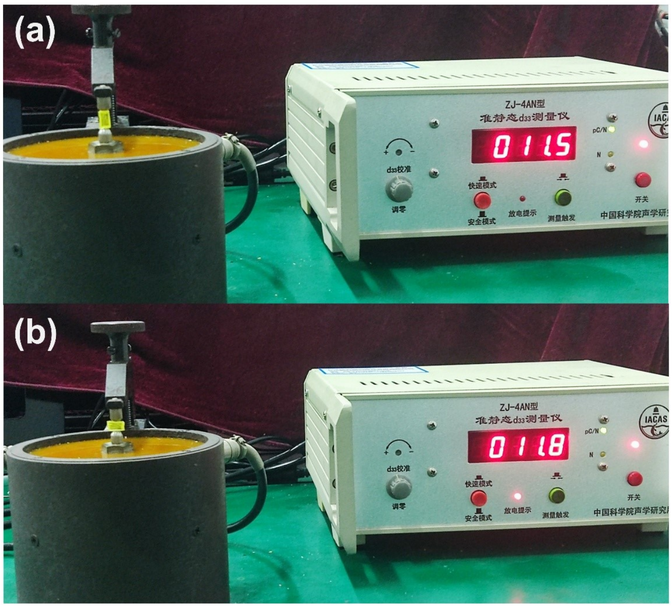

Figure S10. Piezoelectric coefficients along the (a) *c*- and (b) *a*-axis of the SC.

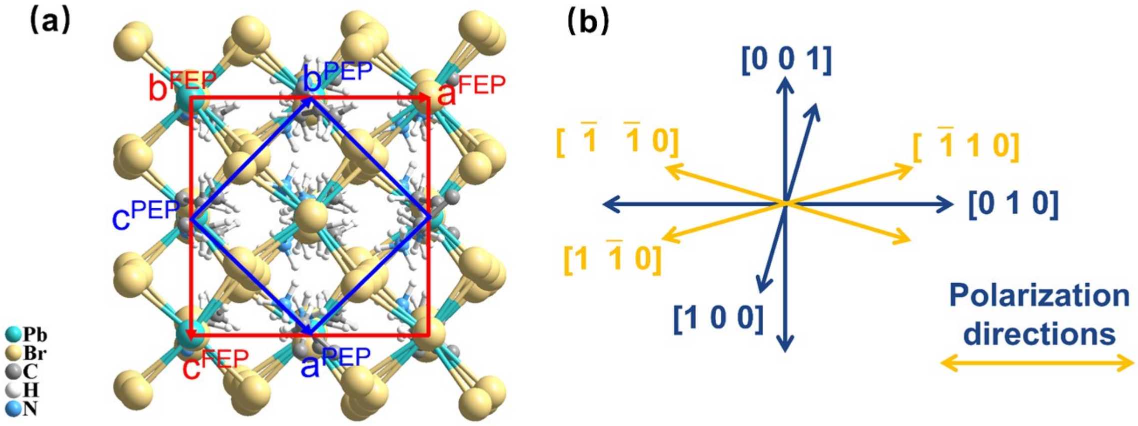

Figure S11. a) Projection of the crystal cell of **1** in the ferroelectric phase, the cell with blue edges representing its tetragonal paraelectric phase; b) Schematic of the four equivalent polarization directions for the ferroelectric species 4/*mmm*→*mm*2.

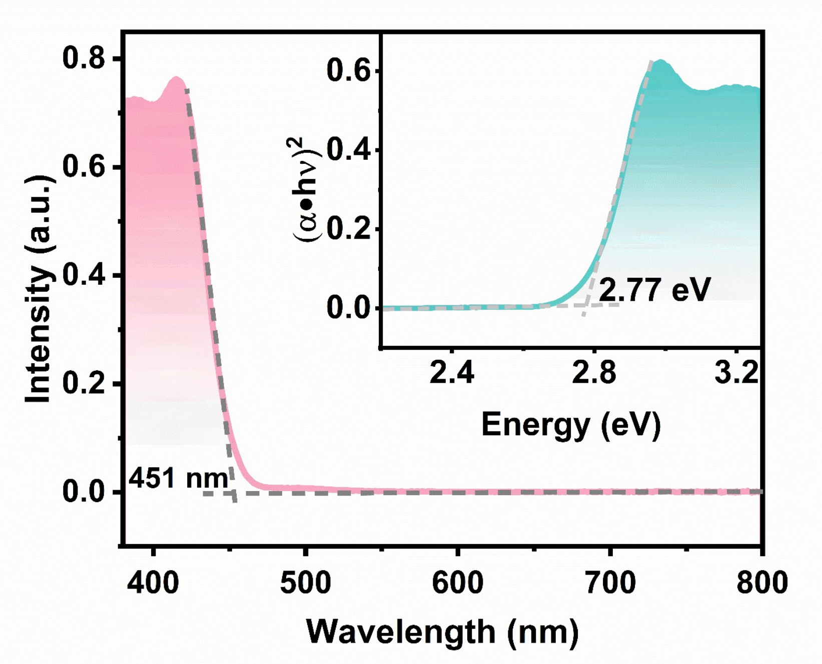

Figure S12. The absorption spectrum and estimated optical bandgap (inset) of **1**.

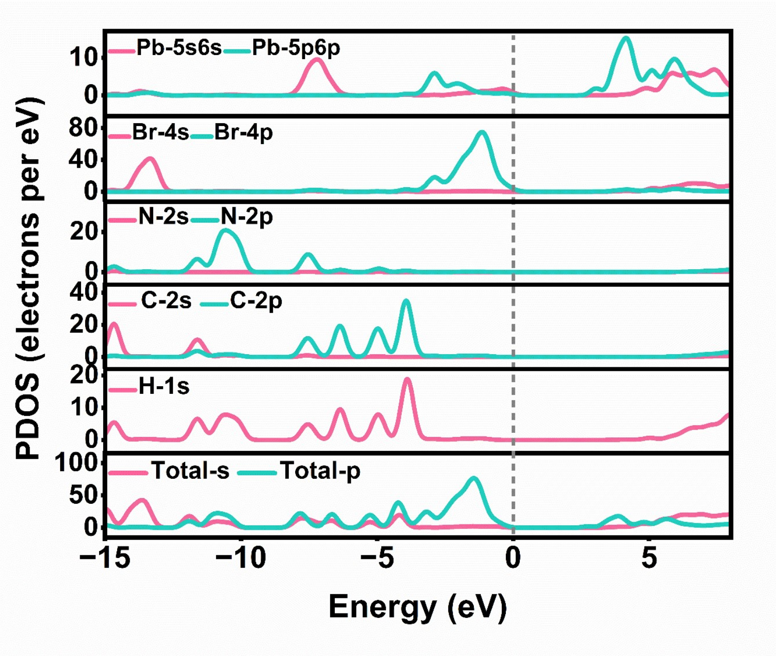

Figure S13. Partial and total DOS profiles of **1**.

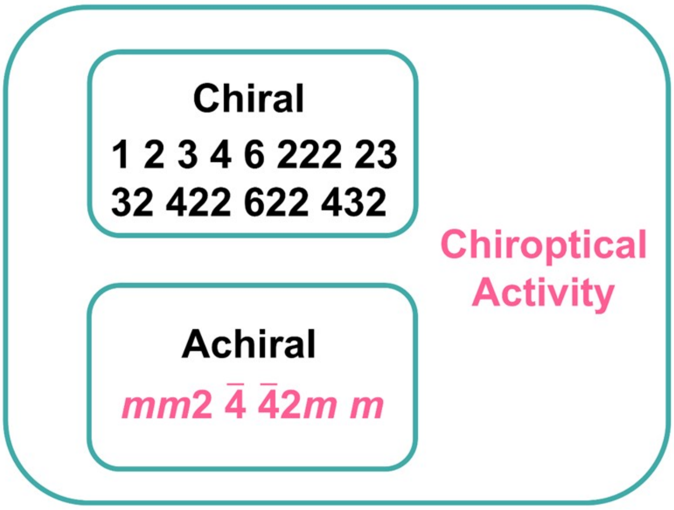

Figure S14. The relationship of chiroptical activity with chirality and achirality.

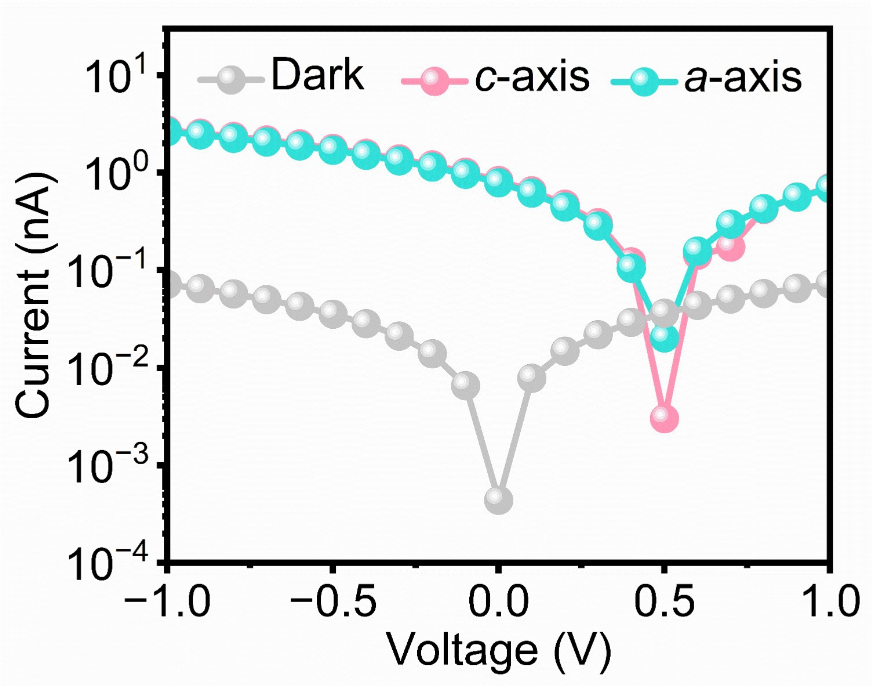

Figure S15. The *I-V* curves of **1** SC device along the *a*-, *c*-axes.

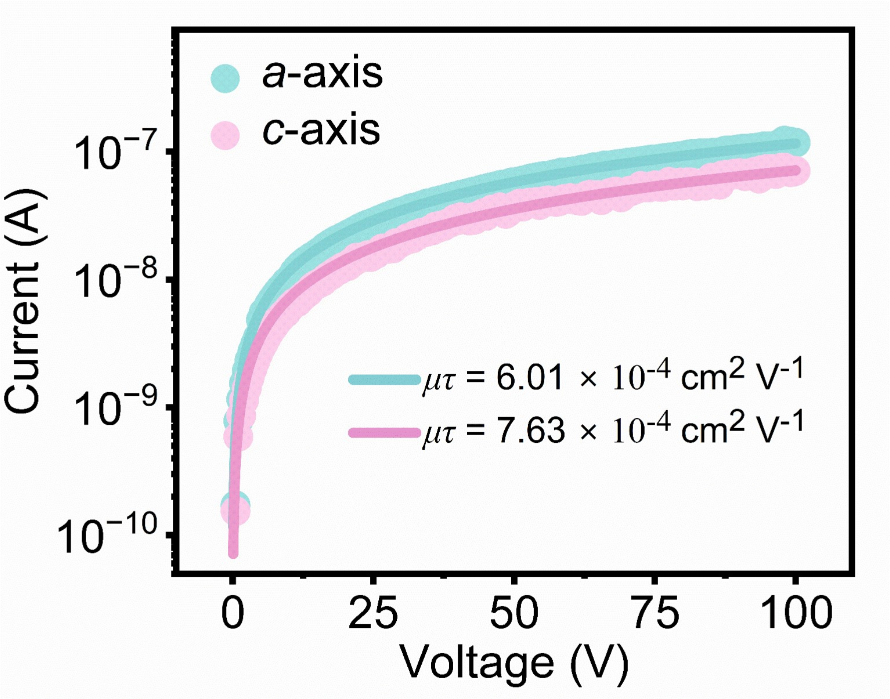

Figure S16. The $\mu\tau$ product under 405 nm illumination.

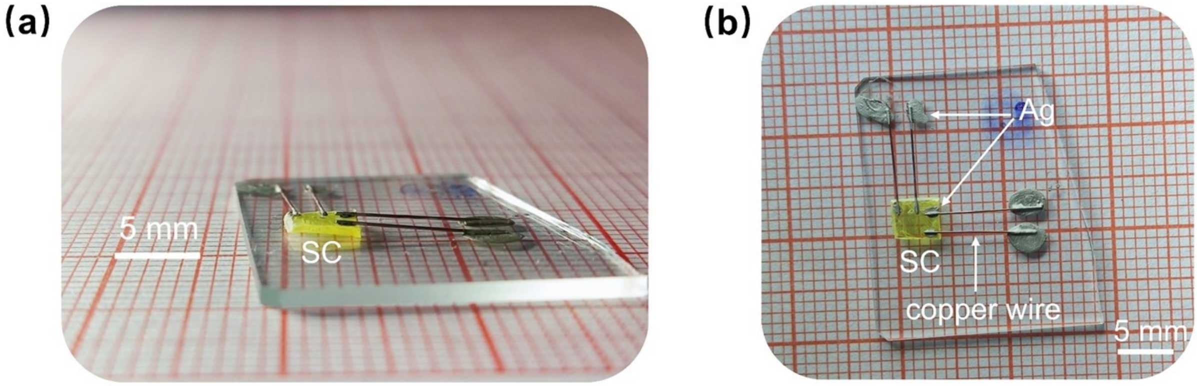

Figure S17. (a) Side view and (b) front view of the single-crystal device **1**.

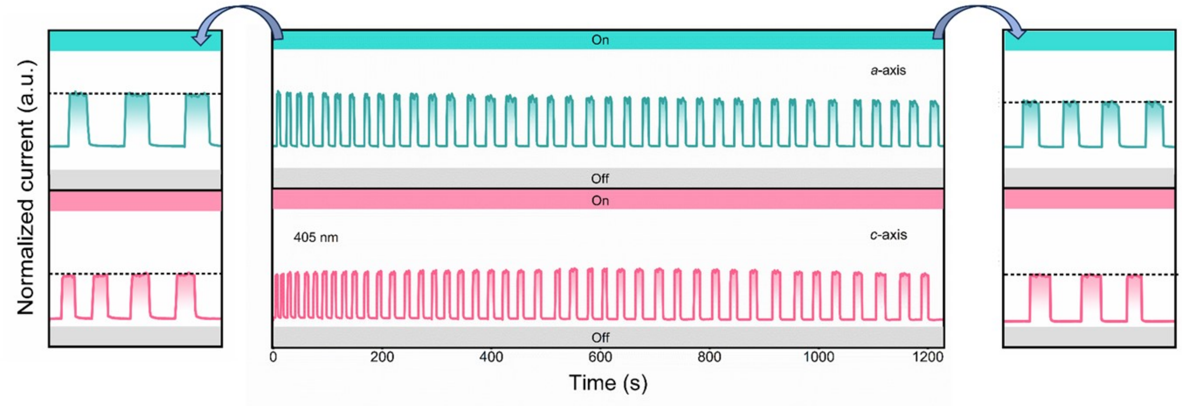

Figure S18. The circle stability of **1**.

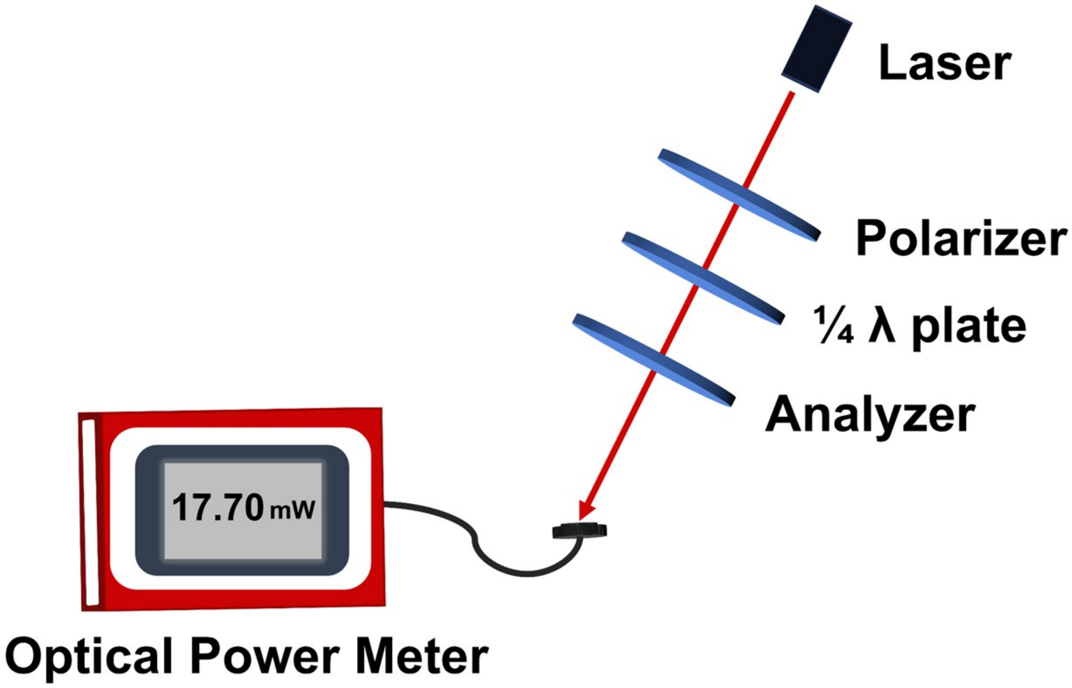

Figure S19. Optical setup diagram for CPL calibration.

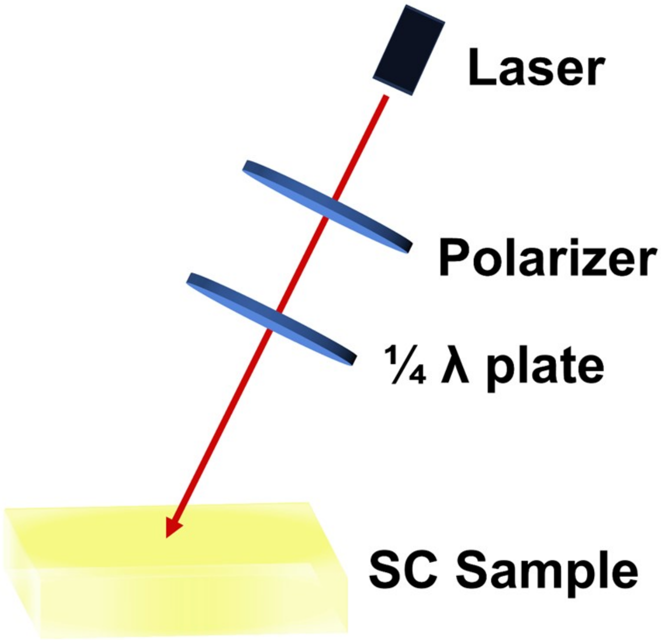

Figure S20. Optical schematic diagram for CPL testing.

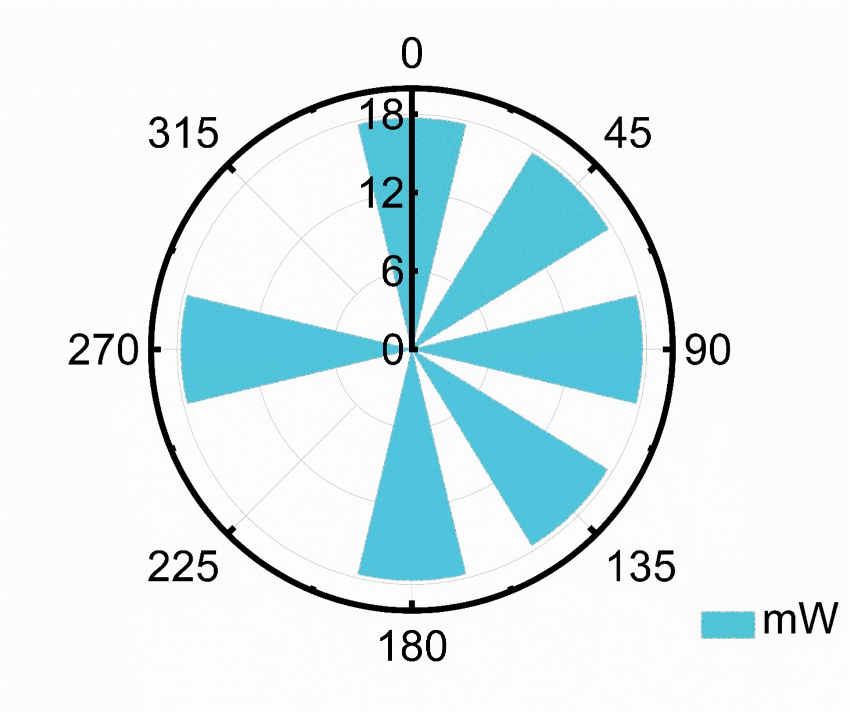

Figure S21. The incident power variation during the analyzer rotation.

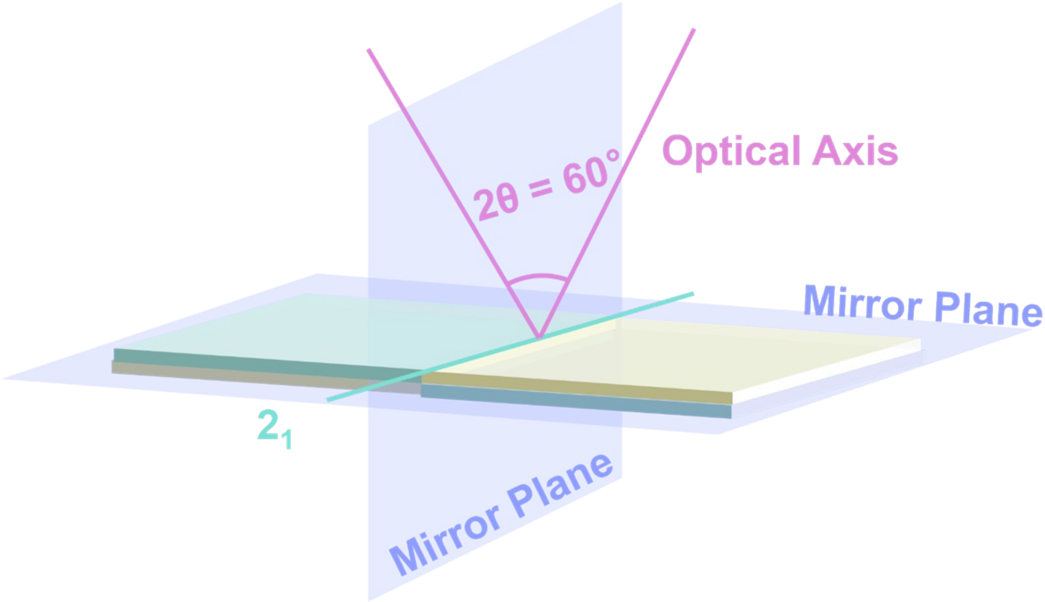

Figure S22. Schematic diagram of **1** crystal with marked symmetry operation: the purple planes represent the mirror planes, the green line is the 2_1 screw axis, and the magenta lines are the two optical axes for the *mm*2 point group. The incident direction of the CPL is along one of the two optic axes for the *mm*2 point group.

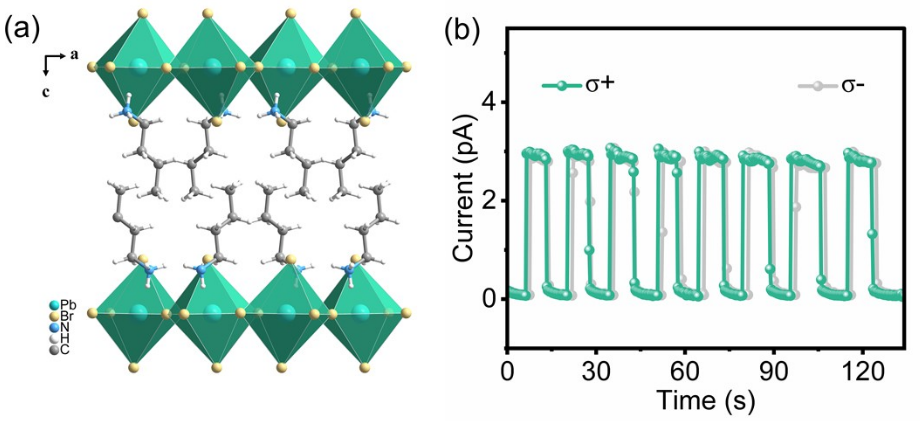

Figure S23. (a) Crystal structure of n-BA_2PbBr_4;(b)Recyclable switching photocurrent of n-BA_2PbBr_4 under left (σ^-) and right (σ^+) CPL with 0.1 V bias at 405 nm (75.4 mW cm^{-2}).

Table S1. Complete Labeling and Component Description.

Label No.	**Component Name**	**Corresponding Parameter**	**Location and Function**
1	Laser	LP405-MF300 (Thorlabs)	Serves as the optical path origin, emitting a stable continuous-wave laser to provide the incident light source for the entire system.
2	Polarizer	LPVISE100-A (Thorlabs)	Convert natural light/unpolarized light into linearly polarized light.
3	1/4 λ plate	WPQ10ME-405 (Thorlabs)	Acts as the core device for converting linearly polarized light to circularly polarized light.
4	Analyzer	LPVISE100-A (Thorlabs)	Detect the polarization state of the light to be measured, which is positioned at the rear end of the optical path (used in the calibration phase).
5	Optical Power Meter	PM100D (Thorlabs)	Measure the intensity of optical radiation (*e.g.*, laser light, polarized light).

Table S2. Asymmetry factors of some reported CPL detectors.

Materials	**Type**	**g_{Iph}**	**Wavelength (nm)**	**Bias (V)**	**Ref.**
$EA_4Pb_3Br_{10}$	Single Crystal	**18% @ *a*-axis**	**405**	**0**	**This work**
		21% @ *c*-axis	**405**	**0**	
$(CPA)_2FAPb_2Br_7$		98%	405	0	1
(4-AMP)BiI_5 (ABI)		24%	405	0	2
$MhyPbBr_3$		39%	405	0	3
$(IBA)_2(EA)_2Pb_3I_{10}$		56%	405	0	4
[(*R*)-PPA]$PAPbBr_4$		50%	405	0	5
[(*R*)-PPA](MOPA)$PbBr_4$		33%	377	0	6
(*S*-BPEA)$_2FAPb_2I_7$		29%	520	0	7
S-[(4-aminophenyl)ethylamine]$_2AgBiI_8\cdot 0.5H_2O$		27%	520	0	8

$[(R)\text{-}\beta\text{-MPA}]_4\mathrm{AgBiI_8}$		30%	520	0	9
$(R\text{-}\beta\text{-MPA})\mathrm{EAPbBr_4}$		19%	405	0	10
$(R/S\text{-3AMP})\mathrm{PbBr_4}$		20%	430	10	11
$R\text{-(BrBA)}_2\mathrm{PbBr_4}$		11%	405	10	12
$[(R)\text{-MBA}]_2\mathrm{PbI_4}$	Film	10%	486	0	13
$(S\text{-MBA})_2\mathrm{MAPb_2I_7}$		9%	505	0	14
$\mathrm{Cs_{0.05}FA_{0.5}MA_{0.45}Pb_{0.5}Sn_{0.5}I_3}$		55%	808	0	15
$\mathrm{RQD}/R\text{-}\mathrm{MBA_2MAPb_2I_7}$		33%	532	0	16
$(S/R\text{-1-2-NEA})\mathrm{MAPb_2I_7}$		15%	405	0	17
$(R/S\text{-BPEA})_2\mathrm{PbI_4}$		4.8%	488	0	18
$(S\text{-MBA})_4\mathrm{Bi_2Br_{10}}$		29%	380	0	19
$(R\text{-}\mathrm{MBA_{0.5}nBA_{0.5}})_2\mathrm{PbI_4}$		58%	510	0	20
$(R\text{-oClPEA})_{0.6}\mathrm{HDA_{0.7}PbI_4}$		12%	483	0	21
$[(R)\text{-}\beta\text{-MPA}]_2\mathrm{MAPb_2I_7}$		20%	532	10	22
$(R\text{-}\alpha\text{-PEA})_2\mathrm{PbI_4/MAPbI_3}$		13%	473	3	23
$(R/S\text{-}\alpha\text{-PEA})\mathrm{PbI_3}$		10%	395	/	24

References

1. X. Li, F. Wu, Y. Yao, W. Wu, C. Ji, L. Li, Z. Sun, J. Luo, X. Liu, *J. Am. Chem. Soc.* 2022, **144**, 14031 - 14036.
2. T. Zhu, J. Bie, C. Ji, X. Zhang, L. Li, X. Liu, X.-Y. Huang, W. Fa, S. Chen, J. Luo, *Nat Commun.* 2022, **13**, 7702.
3. C. Zhang, Z. Wu, W. Zhang, Q. Guan, H. Ye, R. Li, H. Li, Z.-K. Zhu, P. Wang, Y. Wang, Y. Fang, J. Luo, *J. Am. Chem. Soc.* 2025, **147**, 9686 - 9693.
4. Y. Chen, L. Tang, X. Zeng, W. Guo, T. Yang, H. Xu, Y. Liu, G. Gou, Y. Zhao, J. Luo, Z. Sun, *Adv. Funct. Mater.* 2024, **34**, 2311726.
5. Z.-K. Zhu, T. Zhu, S. You, P. Yu, J. Wu, Y. Zeng, Y. Jiang, X. Liu, L. Li, C. Ji, J. Luo, *Adv. Sci.* 2023, **11**, 2307593.
6. Q. Guan, P. Xu, B. Xu, H. Ye, Z. K. Zhu, S. Wang, C. Zhang, H. Li, C. Ji, Z. Lin, J. Luo, *Adv. Sci.* 2025, **12**, 2412506.
7. Q. Guan, Z.-K. Zhu, H. Ye, C. Zhang, H. Li, C. Ji, X. Liu, J. Luo, *Adv. Sci*. 2024, **11**, 2404403.
8. Z. Li, C. Ji, Y. Fan, T. Zhu, S. You, J. Wu, R. Li, Z.-K. Zhu, P. Yu, X. Kuang, J. Luo, *J. Am. Chem. Soc.* 2023, **145**, 25134 - 25142.
9. D. Li, X. Liu, W. Wu, Y. Peng, S. Zhao, L. Li, M. Hong, J. Luo, *Angew. Chem. Int. Ed.* 2021, **60**, 8415 - 8418.
10. W. Wu, L. Li, D. Li, Y. Yao, Z. Xu, X. Liu, M. Hong, J. Luo, *Adv. Opt. Mater.* 2022, **10**, 2102678.
11. C.-C. Fan, X.-B. Han, B.-D. Liang, C. Shi, L.-P. Miao, C.-Y. Chai, C.-D. Liu, Q. Ye, W. Zhang, *Adv. Mater.* 2022, **34**, 2204119.
12. Q. Gu, K. Chen, X. Zhang, S. Wang, S. Wu, W. Huang, *ACS Appl. Mater. Interfaces*. 2025, **17**, 17127 - 17134.
13. J. Wang, H. Lu, X. Pan, J. Xu, H. Liu, X. Liu, D. R. Khanal, M. F. Toney, M. C. Beard, Z. V. Vardeny, *ACS Nano*. 2020, **15**, 588 - 595.
14. H. Wang, L. Yao, Y. Zhan, H. Yu, S. Wu, X. Liu, *ACS Appl. Mater. Interfaces*. 2025, **17**, 3716 - 3724.
15. H. Kim, R. M. Kim, S. D. Namgung, N. H. Cho, J. B. Son, K. Bang, M. Choi, S. K. Kim, K. T. Nam, J. W. Lee, J. H. Oh, *Adv. Sci.* . 2022, **9**, 2104598.
16. J. Yan, X. Zhang, L. Liu, H. Bi, M. Wang, J. Li, J. Wang, *Sci. China Technol. Sci*. 2024, **68**, 1120901.
17. T. Liu, W. Shi, W. Tang, Z. Liu, B. C. Schroeder, O. Fenwick, M. J. Fuchter, *ACS Nano*. 2022, **16**, 2682 - 2689.
18. T. Jeon, D. Yeo, W. Choi, H. Kim, I. H. Jung, J. H. Oh, *J. Mater. Chem. C*. 2024, **12**, 19058 - 19062.
19. A. Maiti, A. J. Pal, *Angew. Chem. Int. Ed.* 2022, **61**, e202214161.
20. X. Zhang, Y. Xu, A. N. Alphenaar, S. Ramakrishnan, Y. Zhang, A. J. Babatunde, Q. Yu, *ACS Nano*. 2024, **18**, 14605 - 14616.
21. H. Song, M. Kwak, W. Choi, D. Yoo, J. H. Oh, *Adv. Opt. Mater.* 2024, **12**, 2401427.
22. L. Wang, Y. Xue, M. Cui, Y. Huang, H. Xu, C. Qin, J. Yang, H. Dai, M. Yuan, *Angew. Chem. Int. Ed.* 2020, **59**, 6442 - 6450.
23. L. Tao, W. Tang, M. Yan, L. Ding, J. Wei, L. Wang, L. Li, L. Li, D. Yang, Y. Fang, *J. Mater. Chem. C*. 2023, **11**, 12392 - 12399.
24. C. Chen, L. Gao, W. Gao, C. Ge, X. Du, Z. Li, Y. Yang, G. Niu, J. Tang, *Nat Commun.* 2019, **10**, 1927.